SPACE OBJECT AREA-TO-MASS RATIO ESTIMATION USING MULTIPLE MODEL APPROACHES

Richard Linares*
University at Buffalo, State University of New York, Amherst, NY, 14260-4400
Moriba K. Jah†
Air Force Research Laboratory, Kirtland AFB, New Mexico, 87117
John L. Crassidis‡
University at Buffalo, State University of New York, Amherst, NY, 14260-4400

In this paper two multiple model approaches are applied to estimate the effective area-to-mass ratio of a space object. Both multiple-model adaptive estimation and a new approach called adaptive likelihood mixtures are used in this work. Multiple model approaches have been used extensively used in target tracking applications since they can detect abrupt changes in the models governing the target's motion. Since the area-to-mass ratio is a function of the projected Sun facing area, which is a function of the orientation of the space object, then the effective area-to-mass ratio is time varying. It is difficult to estimate the time varying nature of the area-to-mass ratio using traditional estimators. Therefore multiple model approaches are proposed here. Simulation results are shown for different scenarios and good performance is given to determine the effective area-to-mass ratios as, well as their changes over time.

INTRODUCTION

In recent years space situational awareness, which is concerned with collecting and maintaining knowledge of all objects orbiting the Earth, has gained much attention. The U.S. Air Force collects the necessary data for space object (SO) catalog development and maintenance through a global network of radars and optical sensors. Due to the fact that a limited number of sensors are available to track a large number of SOs, sparse data collected must be exploited to its fullest extent. Various sensors such as radars and optical sensors exist for SO state estimation, which typically includes position, velocity and a non-conservative force parameter analogous to a ballistic coefficient. However, the ballistic coefficient parameters may not fully describe the SO's motion. Hence, more detailed attitude dependent models are required. In this case more elaborate techniques for processing observation data are required.

There is a coupling between SO attitude and non-conservative force/torques. The acceleration due to solar radiation pressure (SRP) is modeled as function of an object's Sun-facing area, surface properties, mass, position and attitude. It has a very small magnitude compared to gravitational

*Graduate Student, Department of Mechanical & Aerospace Engineering. Email: linares2@buffalo.edu, Student Member AAS.
†Director, Advanced Sciences and Technology Research Institute for Astrodynamics (ASTRIA). Member AAS.
‡Professor, Department of Mechanical & Aerospace Engineering. Email: johnc@buffalo.edu, Member AAS.

accelerations and typically has an order of magnitude around 10^{-7} to 10^{-9} $\mathrm{m/s^2}$, but is the dominant non-conservative acceleration for objects above 1,000 km. Below 1,000 km, drag caused by the atmospheric neutral density is the dominant non-conservative acceleration.

Deep space optical surveys of near geosynchronous (GEO) objects have identified a class of high area-to-mass ratio (HAMR) objects.[1] The exact characteristics of these objects are not well known and their motion pose a collision hazard with GEO objects due the SRP induced large variations of inclination and eccentricity. These objects are typically non-resolved and difficult to track due to dim magnitude and dynamic mismodeling. Therefore, characterizing the large population of HAMR objects in geostationary orbit is required to allow for a better understanding of their origins, and the current and future threats they pose to the active SO population.

Estimating the dynamic characteristics of a HAMR object using light curve and astrometric data can allow for mass parameters to be observable. Estimating mass for HAMR objects can help in the development of a detailed understanding of the origin and dynamics of these objects. It has been shown that the SRP albedo area-to-mass ratio, $\frac{C_r \mathcal{A}}{m}$, is observable from angles data[2] through the dynamic mismodeling of SRP forces. Reference [2] conducts a study with simulated and actual data to quantify the error in the estimates of $\frac{C_r \mathcal{A}}{m}$ and good performance is found using data spanning over a number of months. Also Ref. [3] shows that orbital, attitude and shape parameters can be recovered with sufficient accuracy using a multiple-model adaptive estimation approach coupled with an unscented Kalman filter. This approach works reasonably well but requires that the area-to-mass ratio is known *a priori*. The purpose of this work is to show that since $\frac{C_r \mathcal{A}}{m}$ is observable from angles data and shape/albedo properties are observable from photometric data, then by fusing these data types, the area-to-mass ratio can be extracted with reasonable accuracy.

Filtering algorithms for state estimation, such as the extended Kalman filter (EKF),[4] the unscented Kalman filter (UKF)[5] and particle filters[6] are commonly used to both estimate hidden (indirectly observable) states and filter noisy measurements. The basic difference between the EKF and the UKF results from the manner in which the state distribution of the nonlinear models is approximated. The UKF, introduced by Julier and Uhlmann,[5] uses a nonlinear transformation called the unscented transform, in which the state probability density function (pdf) is represented by a set of weighted sigma points (state vectors deterministically sampled about a mean). These are used to parameterize the true mean and covariance of the state distribution. When the sigma points are propagated through the nonlinear system, the posterior mean and covariance are obtained up to the second order for any nonlinearity. The EKF and UKF assume that the process noise terms are represented by zero-mean Gaussian white-noise processes and the measurement noise is represented by zero-mean Gaussian random variable. Furthermore both approaches assume that the *a posteriori* and *a priori* pdf is Gaussian in a linear domain. This is true given the previous assumptions but under the effect of nonlinear measurement functions and system dynamics the initial Gaussian state uncertainty may quickly become non-Gaussian. Both filters only provide approximate solutions to the nonlinear filtering problem, since the *a posteriori* and *a priori* pdf are most often non-Gaussian due to nonlinear effects. The EKF typically works well only in the region where the first-order Taylor-series linearization adequately approximates the non-Gaussian pdf. The UKF provides higher-order moments for the computation of the *a posteriori* pdf without the need to calculate Jacobian matrices as required in the EKF. The light curve measurement model is highly nonlinear, and Jacobian calculations are non-trivial; thus, the UKF is used to provide a numerical means of estimating the states of the SO using light curve measurement models.

In this paper the usefulness of the information taken by optical sensors is investigated with the

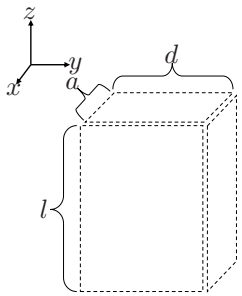

Figure 1. Space Object Shape Model

UKF and adaptive filtering techniques to determine the area-to-mass ratio. The standard multiple-model adaptive estimation (MMAE) approach is applied to characterize the area-to-mass ratio of an SO, given angles data. Also a technique call adaptive likelihood mixtures (ALM) is presented and applied to characterizing the area-to-mass ratio. This approach works by weighting each model with the current likelihood ratio and therefore the weights are not functions of the previous weights which removes the memory of the multiple model approach. This ALM approach can then detect very abrupt changes in the data and is flexible enough to determine the correct corresponding model. Since the area-to-mass ratio is a function of the projected area of the SO which is a function of the orientation of SO, then the effective area-to-mass ratio is time varying. This time variation is difficult to capture in traditional estimators, so the aforementioned multiple model approaches are proposed to capture the transition between simplified cannonball models.

The organization of this paper is as follows. First, the models used for SO shape, orbital dynamics and attitude dynamics are discussed. Following this a description of the measurement models used in this paper are given. Next, a review of the UKF approach is provided. Then both multiple model approaches are discussed. Finally, simulation results of the area-to-mass estimation approach are provided.

SHAPE MODEL

The shape model considered in this work consists of a finite number a flat facets, where each facet has a set of basis vectors associated with it. These basis vectors consist of three unit vectors $\mathbf{u}_n^B$, $\mathbf{u}_u^B$, and $\mathbf{u}_v^B$. The unit vector $\mathbf{u}_n^B$ points in the direction of the outward normal to the facet. For curved surfaces this model become more accurate as the number of facets are increased. The vectors $\mathbf{u}_u^B$ and $\mathbf{u}_v^B$ are in the plane of the facet, the notation superscript B denotes that the vector is expressed in body coordinates. The SOs are assumed to be rigid bodies and therefore the unit vectors $\mathbf{u}_n^B$, $\mathbf{u}_u^B$ and $\mathbf{u}_v^B$ do not change since they are expressed in the body frame.

The light curve and the solar radiation pressure models discussed in the next sections require that these vectors be expressed in inertial coordinates and since the SO body is rotating, these vectors will change with respect to the inertial frame. The body vectors can be rotated to the inertial frame by the standard attitude mapping given by:

$$\mathbf{u}_i^B = A(\mathbf{q}_I^B)\mathbf{u}_k^I, \quad k = u,\, v,\, n, \tag{1}$$

where $A(\mathbf{q}_I^B)$ is the attitude matrix mapping the inertial frame to the body frame using the quaternion parameterization. Furthermore, the unit vector $\mathbf{u}_{\text{sun}}^I$ points from the SO to the Sun direction

and the unit vector $\mathbf{u}^I_{\text{obs}}$ points from the SO to the observer. Each facet has an area $\mathcal{A}(i)$ associated with it. Once the number of facets has been defined and their basis vectors are known, the areas $\mathcal{A}(i)$ define the size and shape of the SO. To determine the solar radiation pressure forces and light curve characteristics, the surface properties must be defined for each facet.

For the development of the measured light curve data, faceted SO shape models are used. The rectangular model is described by three parameters, l, a, and d, which are the length, width, and height, respectively.

DYNAMIC MODELS

The two-body equation of motion with solar radiation pressure (SRP) accelerations is given by

$$\ddot{\mathbf{r}}^I = -\frac{\mu}{r^3}\mathbf{r}^I + \mathbf{a}^I_{\text{srp}}, \tag{2}$$

where μ is the gravitational parameter of the Earth, $r = \|\mathbf{r}^I\|$, and $\mathbf{a}^I_{\text{srp}}$ represents the acceleration perturbation due to SRP, which will be discussed in detail in the following section. The superscript I denotes that the vectors are expressed in inertial coordinates

A number of parameterizations exist to specify attitude, including Euler angles, quaternions and Rodrigues parameters.[7] This paper uses the quaternion, which is based on the Euler angle/axis parametrization. The quaternion is defined as $\mathbf{q} \equiv [\boldsymbol{\varrho}^T \quad q_4]^T$ with $\boldsymbol{\varrho} = \hat{\mathbf{e}}\sin(\nu/2)$, and $q_4 = \cos(\nu/2)$, where $\hat{\mathbf{e}}$ and ν are the Euler axis of rotation and rotation angle, respectively. The quaternion must satisfy a unit norm constraint, $\mathbf{q}^T\mathbf{q} = 1$. In terms of the quaternion, the attitude matrix is given by

$$A(\mathbf{q}) = \Xi^T(\mathbf{q})\Psi(\mathbf{q}), \tag{3}$$

where

$$\Xi(\mathbf{q}) \equiv \begin{bmatrix} q_4 I_{3\times 3} + [\boldsymbol{\varrho}\times] \\ -\boldsymbol{\varrho}^T \end{bmatrix}, \tag{4a}$$

$$\Psi(\mathbf{q}) \equiv \begin{bmatrix} q_4 I_{3\times 3} - [\boldsymbol{\varrho}\times] \\ -\boldsymbol{\varrho}^T \end{bmatrix}, \tag{4b}$$

with

$$[\mathbf{a}\times] \equiv \begin{bmatrix} 0 & -a_3 & a_2 \\ a_3 & 0 & -a_1 \\ -a_2 & a_1 & 0 \end{bmatrix} \tag{5}$$

for any general 3×1 vector $\mathbf{a}$ defined such that the matrix form is equivalent to the vector cross product $[\mathbf{a}\times]\mathbf{b} = \mathbf{a} \times \mathbf{b}$.

The rotational dynamics are given by the coupled first-order differential equations:

$$\dot{\mathbf{q}}^B_I = \frac{1}{2}\Xi(\mathbf{q}^B_I)\boldsymbol{\omega}^B_{B/I}, \tag{6a}$$

$$\dot{\boldsymbol{\omega}}^B_{B/I} = J^{-1}_{\text{SO}}\left(\mathbf{T}^B_{\text{srp}} - \left[\boldsymbol{\omega}^B_{B/I}\times\right] J_{\text{SO}}\boldsymbol{\omega}^B_{B/I}\right), \tag{6b}$$

where $\boldsymbol{\omega}^B_{B/I}$ is the angular velocity of the SO with respect to the inertial frame, expressed in body coordinates (the notation superscript B denotes that the vector is expressed in body coordinates),

J_{SO} is the inertia matrix of the SO and $\mathbf{T}_{\text{srp}}^{B}$ is the net torque acting on the SO due to SRP expressed in body coordinates.

The SO is assumed to be of uniform density and therefore the principal components of the inertia tensor for the shape model given in Figure 1 are given by

$$J_1 = m_{SO}\frac{\left(a^2+b^2\right)}{12} \tag{7a}$$

$$J_2 = m_{SO}\frac{\left(a^2+l^2\right)}{12} \tag{7b}$$

$$J_3 = m_{SO}\frac{\left(l^2+b^2\right)}{12} \tag{7c}$$

Then the inertia matrix is given by $J_{\text{SO}} = \text{diag}\left[J_1 \;\; J_2 \;\; J_3\right]$. This work will consider simplified SRP models which consider the SO to be of spherical shape and therefore the SRP force does not depend on orientation. In most cases this simplification is an approximation and therefore one of the simulation scenarios will consider the shape model discussed earlier and simulation the rotational dynamics using Eq. 6 to generate truth data and process the data with an estimator that assumes spherical shapes.

SOLAR RADIATION FORCE MODEL

For higher altitude objects ($\geq$ 1,000 km) SRP represents the primary non-conservative perturbation acting on SOs. Because SRP depends upon the SO's position and orientation, the position and attitude dynamics are thus coupled. The acceleration due to SRP is computed as a function of the total solar energy impressed upon exposed SO surfaces that are reflected, absorbed and reradiated. The rate at which radiant energy is incident on an element of area $d\mathcal{A}$ is a function of angle between the normal to $d\mathcal{A}$, $\mathbf{u}_n$, and the Sun direction $\mathbf{u}_{\text{sun}}$. The power of incident radiant energy is given by

$$P_I = \frac{\Phi_{\text{sun,tot}}}{(d/d_0)^2}\left(\mathbf{u}_n \cdot \mathbf{u}_{\text{sun}}\right) d\mathcal{A} \tag{8}$$

where $\Phi_{\text{sun,tot}}$ is the average incident radiant flux density from the Sun at 1 AU, given by $\Phi_{\text{sun,tot}} = 1,367\ \text{W/m}^2$. Therefore the energy flux at any distance d is given by $\Phi_{\text{sun,tot}}/(d/d_0)^2$ where $d_0 = 1$ AU. The reflected radiation will have the following diffuse and specular power:

$$P_D = C_{\text{diff}}\frac{\Phi_{\text{sun,tot}}}{(d/d_0)^2}\left(\mathbf{u}_n \cdot \mathbf{u}_{\text{sun}}\right) d\mathcal{A} \tag{9a}$$

$$P_S = C_{\text{spec}}\frac{\Phi_{\text{sun,tot}}}{(d/d_0)^2}\left(\mathbf{u}_n \cdot \mathbf{u}_{\text{sun}}\right) d\mathcal{A} \tag{9b}$$

where the incident solar radiant energy is accounted for in three terms: the absorbed energy, C_{abs}, the specularly reflected energy C_{spec}, and the diffusely reflected energy, C_{diff}, which yields

$$C_{\text{abs}} + C_{\text{spec}} + C_{\text{diff}} = 1 \tag{10}$$

The elemental force on $d\mathcal{A}$ can be written in three terms: incident force, $\mathbf{dF}_I$, specular reflection force, $\mathbf{dF}_S$, and diffuse reflection force, $\mathbf{dF}_D$. The incident force accounts for force due to the three terms C_{abs}, C_{spec}, and C_{diff}, since for each term the radiant particle is at least brought to rest before being absorbed or reflected. Therefore, $\mathbf{dF}_I$ accounts for the transfer in momentum to

bring a radiated particle to rest. The force term for diffuse and specular reflectance accounts for the momentum transfer due to reflection. The momentum contribution due to incident energy is in the opposite direction of the incoming energy, given by

$$\mathbf{dF}_I = -\frac{P_I}{c}\mathbf{u}_n \tag{11}$$

The force exerted by specularly reflected energy is in the direction of specular reflection which is given by reflecting the vector $\mathbf{u}_{\text{sun}}$ about an axis defined by the direction $\mathbf{u}_n$. Then the force exerted by specular reflection is given by

$$\mathbf{dF}_S = \frac{P_S}{c}\left[2\left(\mathbf{u}_n \cdot \mathbf{u}_{\text{sun}}\right)\mathbf{u}_n - \mathbf{u}_{\text{sun}}\right] \tag{12}$$

Diffusely reflected energy will reflect equally in all directions and the resulting force will be in the normal direction due to symmetric components canceling out. For surfaces obeying Lambert's cosine law of diffuse emission the diffuse term will be[8]

$$\mathbf{dF}_D = \frac{2}{3}\frac{P_D}{c}\mathbf{u}_n \tag{13}$$

where the factor $\frac{2}{3}$ accounts for the portion of energy that is reflected in the normal direction. Then the force on an element of area is given by

$$\mathbf{dF} = \mathbf{dF}_I + \mathbf{dF}_S + \mathbf{dF}_D \tag{14}$$

The force acting on a body due to solar radiation pressure can be determined by integrating over the Sun exposed surface area, given by

$$\mathbf{F} = \int_{\text{sun}} \left(\mathbf{dF}_I + \mathbf{dF}_S + \mathbf{dF}_D\right) \tag{15}$$

For a spherical body this integral is calculated over the Sun exposed area. The result is given by

$$\mathbf{F} = -\frac{\Phi_{\text{sun,tot}}}{c(d/d_0)^2}\mathcal{A}\left[1 + \frac{2}{3}C_{\text{diff}}\right]\mathbf{u}_{\text{sun}} \tag{16}$$

This equation can be rewritten in terms of albedo

$$\mathbf{F} = -\frac{\Phi_{\text{sun,tot}}}{c(d/d_0)^2}\mathcal{A}C_r\mathbf{u}_{\text{sun}} \tag{17}$$

where $C_r = 1 + \frac{2}{3}C_{\text{diff}}$. Similarly the forces can be calculated for a flat plate:

$$\begin{aligned}\mathbf{F} = -\frac{\Phi_{\text{sun,tot}}}{c(d/d_0)^2}\mathcal{A}\left(\mathbf{u}_n \cdot \mathbf{u}_{\text{sun}}\right)\Bigg[&\left(1 - C_{\text{spec}}\right)\mathbf{u}_n \\ &+ \left(\frac{4}{9}C_{\text{diff}} + 2C_{\text{spec}}\left(\mathbf{u}_n \cdot \mathbf{u}_{\text{sun}}\right)\right)\mathbf{u}_{\text{sun}}\Bigg]\end{aligned} \tag{18}$$

Under the assumption of a perfectly diffuse flat plate, Eq. (18) becomes

$$\mathbf{F} = -\frac{\Phi_{\text{sun,tot}}}{c(d/d_0)^2}\left(\mathbf{u}_n \cdot \mathbf{u}_{sun}\right)\left[\mathcal{A}\,\mathbf{u}_n + \frac{4}{9}\mathcal{A}\,C_{\text{diff}}\,\mathbf{u}_{\text{sun}}\right] \tag{19}$$

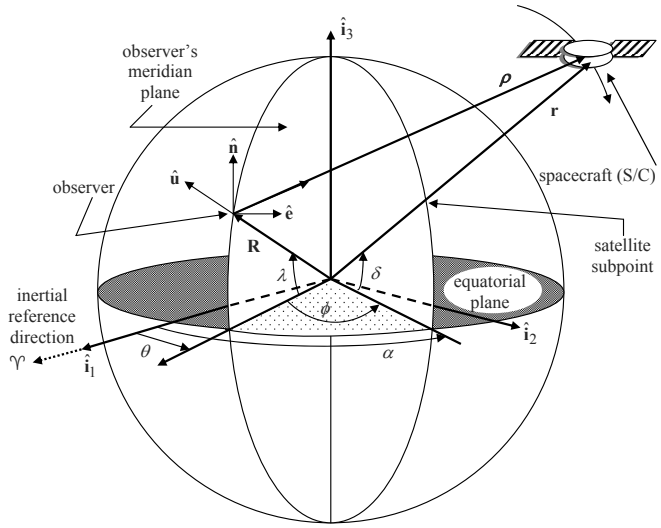

Figure 2. Geometry of Earth Observations of Spacecraft Motion

We can note that, if $\mathbf{u}_n$ remains aligned with $\mathbf{u}_{\text{sun}}$, a similar expression to Eq. (17) can be written for the flat plate model, where $C_r = 1 + \frac{4}{9}C_{\text{diff}}$ in the case of the flat plate. To calculate the SRP force for the facet model discussed previously, the SRP force is calculated for each facet using the SRP force equation for a flat plate, Eq. (19), and then summed over all facets to obtain the total SRP force on the body:

$$\mathbf{F}^I_{\text{srp}} = \sum_{j=1}^{N_F} \mathbf{F}^I_{\text{srp},j} \tag{20}$$

where N_F is the total number of facets. The sum is performed over all sides of the SO. If for any side the angle between the surface normal and the Sun's direction is greater than $\pi/2$, then this side is not facing the Sun and receives no energy from the Sun. Therefore, the solar radiation pressure for these sides is set to zero, $\mathbf{F}^I_{\text{srp},j} = \mathbf{0}$ if $\theta_{\text{inc}} > \pi/2$. The acceleration due to SRP is then simply given by $\mathbf{a}^I_{\text{srp}} = \mathbf{F}^I_{\text{srp}}/m$.

The solar radiation pressure moments can be calculated by assuming that the SRP force acts through the center of each facet. Then the SRP moments can be written as

$$\mathbf{T}^B_{\text{srp}} = \sum_{j=1}^{N_F} \left[\mathbf{r}^B_i \times\right] A\mathbf{F}^B_{\text{srp},j} \tag{21}$$

where $\mathbf{r}^B_i$ is the location of the geometric center of each facet with respect to the center of mass of the SO in body coordinates. The SRP moments are used with Eq. (6) to simulate the rotational dynamics of the SO.

ORBIT DETERMINATION USING UNSCENTED KALMAN FILTER

Observation Model

Consider observations made by a optical site which measures the right ascension and declination to a SO. The geometry and common terminology associated with this observation is shown in Figure

2, where $\mathbf{d}^I$ is the position vector from the observer to the SO, $\mathbf{r}^I$ is the position of the SO in inertial coordinates, $\mathbf{R}^I$ is the radius vector locating the observer. The fundamental observation is given by

$$\boldsymbol{\rho}^I = \mathbf{r}^I - \mathbf{R}^I \tag{22}$$

where $\boldsymbol{\rho} = [\rho_x \ \rho_y \ \rho_z]^T$. The angle observations consist of the right ascension, ra, and declination, dec. The observation equations are given by

$$\text{ra} = \tan^{-1}\left(\frac{\rho_x}{\rho_y}\right) \tag{23a}$$

$$\text{dec} = \sin^{-1}\left(\frac{\rho_z}{\|\rho^I\|}\right) \tag{23b}$$

UNSCENTED KALMAN FILTER FORMULATION

The unscented Kalman filter (UKF) is chosen for state estimation because it has at least the accuracy of a second-order filter[5] without the requirement of computing Jacobians like the EKF.

Model and Measurement Uncertainty

A UKF is now summarized for estimating the state of a SO's position, velocity given by $\mathbf{x} = [\mathbf{r}^{I^T} \ \mathbf{v}^{I^T}]^T$. The dynamic models from Eqs. (2) and (6) can be written in the general state equation which gives the deterministic part of the stochastic model:

$$\dot{\mathbf{x}} = \mathbf{f}\left(\mathbf{x}, t\right) + G\left(\mathbf{x}, t\right)\boldsymbol{\Gamma}(t) \tag{24}$$

where $\boldsymbol{\Gamma}(t)$ is a Gaussian white noise process term with correlation function $Q\delta(t_1 - t_2)$. The function $\mathbf{f}\left(\mathbf{x}, t\right)$ is a general nonlinear function. To solve the general nonlinear filtering problem the UKF utilizes the unscented transformation to determine the mean and covariance propagation though the function $\mathbf{f}\left(\mathbf{x}, t\right)$. The dynamic function used in this work consists of rotational and translational dynamics given by the sigma points, which are propagated through the system dynamics:

$$\mathbf{f}\left([\boldsymbol{\chi}, \hat{\mathbf{q}}]\right) = \begin{bmatrix} \hat{\mathbf{v}}^I \\ -\dfrac{\mu}{r^3}\hat{\mathbf{r}}^I + \hat{\mathbf{a}}^I_{\text{SRP}} \end{bmatrix} \tag{25}$$

If the initial pdf $p(\mathbf{x}_o)$ that describes the associated state uncertainty is given, the solution for the time evolution of $p(\mathbf{x}, t)$ constitutes the nonlinear filtering problem.

Given a system model with initial state and covariance values, the UKF propagates the state vector and the error-covariance matrix recursively. At discrete observation times, the UKF updates the state and covariance matrix conditioned on the information gained from the measurements. The prediction phase is important for overall filter performance. In general, the discrete measurement equation can be expressed for the filter as

$$\tilde{\mathbf{y}}_k = \mathbf{h}\left(\mathbf{x}_k, t_k\right) + \mathbf{v}_k \tag{26}$$

where $\tilde{\mathbf{y}}_k$ is a measurement vector and $\mathbf{v}_k$ is the measurement noise, which is assumed to be a zero-mean Gaussian process with covariance R_k.

All random variables in the UKF are assumed to be Gaussian random variables and their distribution are approximated by the deterministically selected sigma points. The sigma points are

selected to be along the principal axis directions of the state error-covariance. Given an $L \times L$ error-covariance matrix P_k, the sigma points are constructed by

$$\boldsymbol{\sigma}_k \leftarrow 2L \text{ columns from } \pm\sqrt{(L+\lambda)P_k} \tag{27a}$$

$$\boldsymbol{\chi}_k(0) = \boldsymbol{\mu}_k \tag{27b}$$

$$\boldsymbol{\chi}_k(i) = \boldsymbol{\sigma}_k(i) + \boldsymbol{\mu}_k \tag{27c}$$

where $\sqrt{M}$ is shorthand notation for a matrix Z such that $M = Z\,Z^T$. Given that these points are selected to represent the distribution of the state vector, each sigma point is given a weight that preserves the information contained in the initial distribution:

$$W_0^{\text{mean}} = \frac{\lambda}{L+\lambda} \tag{28a}$$

$$W_0^{\text{cov}} = \frac{\lambda}{L+\lambda} + (1 - \alpha^2 + \beta) \tag{28b}$$

$$W_i^{\text{mean}} = W_i^{\text{cov}} = \frac{1}{2(L+\lambda)}, \quad i = 1,\, 2,\, \ldots,\, 2L \tag{28c}$$

where $\lambda = \alpha^2(L+\kappa) - L$ is a composite scaling parameter.

The constant α controls the spread of the sigma point distribution and should be a small number, $0 < \alpha \leq 1$. $\kappa = 3 - L$ provides an extra degree of freedom that is used to fine-tune the higher-order moments, and β is used to incorporate prior knowledge of the distribution by weighting the mean sigma point in the covariance calculation.

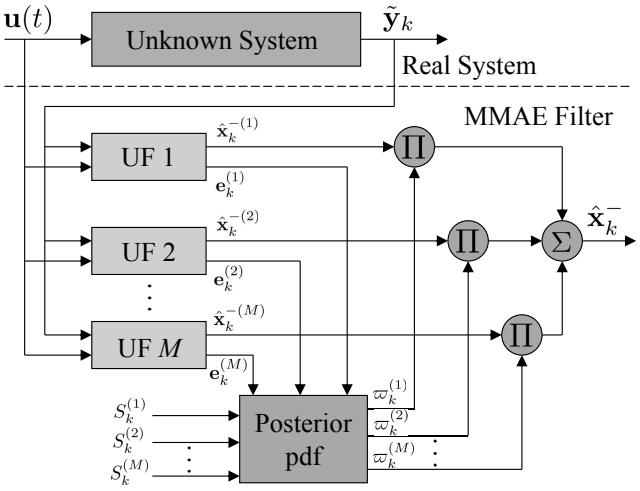

Figure 3. MMAE Process

MULTIPLE-MODEL ADAPTIVE ESTIMATION

In this section a review of MMAE is shown. More details can be found in Refs. [9] and [10]. Figure 3 shows the MMAE process. Multiple-model adaptive estimation is a recursive estimator

that uses a bank of filters that depend on models with different parameters, denoted by the vector $\mathbf{p}$, which is assumed to be constant (at least throughout the interval of adaptation). Note the stationary assumption for the state and/or output processes is not necessarily required though, i.e. time varying state and output matrices can be used. A set of distributed elements is generated from some known pdf of $\mathbf{p}$, denoted by $p(\mathbf{p})$, to give $\{\mathbf{p}^{(\ell)};\, \ell = 1,\, \ldots,\, M\}$. The finite set of parameters can be the results of discretizing a continuous parameters space, selecting a set of values $\{\mathbf{p}^{(1)},\, \mathbf{p}^{(2)},\, \ldots,\, \mathbf{p}^{(k)}\}$ dispersed throughout the region of reasonable parameter values.

The goal of the estimation process is to determine the conditional pdf of the ℓ^{th} element, $\mathbf{p}^{(\ell)}$, given all the measurements. Application of Bayes' rule yields

$$p(\mathbf{p}^{(\ell)}|\tilde{\mathbf{Y}}_k) = \frac{p(\tilde{\mathbf{Y}}_k|\mathbf{p}^{(\ell)})\, p(\mathbf{p}^{(\ell)})}{\sum_{j=1}^{M} p(\tilde{\mathbf{Y}}_k|\mathbf{p}^{(j)})\, p(\mathbf{p}^{(j)})} \tag{29}$$

where $\tilde{\mathbf{Y}}_k$ denotes the sequence $\{\tilde{\mathbf{y}}_0,\, \tilde{\mathbf{y}}_1,\, \ldots,\, \tilde{\mathbf{y}}_k\}$. The conditional probability $p(\mathbf{p}^{(\ell)}|\tilde{\mathbf{Y}}_k)$ will be the metric used to select the most likely model and or the most likely combination of shape models. The *a posteriori* probabilities can be computed through[11]

$$\begin{aligned} p(\mathbf{p}^{(\ell)}|\tilde{\mathbf{Y}}_k) &= \frac{p(\tilde{\mathbf{y}}_k,\, \mathbf{p}^{(\ell)}|\tilde{\mathbf{Y}}_{k-1})}{p(\tilde{\mathbf{y}}_k|\tilde{\mathbf{Y}}_{k-1})} \\ &= \frac{p(\tilde{\mathbf{y}}_k|\hat{\mathbf{x}}_k^{-(\ell)})\, p(\mathbf{p}^{(\ell)}|\tilde{\mathbf{Y}}_{k-1})}{\sum_{j=1}^{M} \left[p(\tilde{\mathbf{Y}}_k|\hat{\mathbf{x}}_k^{-(j)})\, p(\mathbf{p}^{(j)}|\tilde{\mathbf{Y}}_{k-1})\right]} \end{aligned} \tag{30}$$

The conditional probability densities of the observations based on each hypothesis (likelihood) $p(\tilde{\mathbf{y}}_k|\hat{\mathbf{x}}_k^{-(\ell)})$ are given as

$$p(\tilde{\mathbf{y}}_k|\hat{\mathbf{x}}_k^{-(\ell)}) = \frac{1}{\det\left(2\pi S_k^{(\ell)}\right)^{1/2}} \exp\left\{-\frac{1}{2}\mathbf{e}_k^{(\ell)T} S_k^{(\ell)} \mathbf{e}_k^{(\ell)}\right\} \tag{31}$$

where measurement residual for the ℓ^{th} hypothesis (model) is given by

$$\mathbf{e}_k^{(\ell)} = \tilde{\mathbf{y}}_k - \mathbf{h}[\hat{\mathbf{x}}_k^{-}(\mathbf{p}^{(\ell)})] \tag{32}$$

and corresponding residual (innovations) covariance matrix from the UKF, denoted by $S_k^{(\ell)}$, given from the ℓ^{th} filter.

Note that the denominator of Eq. (30) is just a normalizing factor to ensure that $p(\mathbf{p}^{(\ell)}|\tilde{\mathbf{Y}}_k)$ is a pdf. The recursion formula can now be cast into a set of defined weights $\varpi_k^{(\ell)}$, so that

$$\begin{aligned} \varpi_k^{(\ell)} &= \varpi_{k-1}^{(\ell)} p(\tilde{\mathbf{y}}_{k-1}|\hat{\mathbf{x}}_{k-1}^{+(\ell)}) \\ \varpi_k^{(\ell)} &\leftarrow \frac{\varpi_k^{(\ell)}}{\sum_{j=1}^{M} \varpi_k^{(j)}} \end{aligned} \tag{33}$$

where $\varpi_k^{(\ell)} \equiv p\left(\mathbf{p}^{(\ell)}|\tilde{\mathbf{y}}_k\right)$. Note that only the current time measurement $\tilde{\mathbf{y}}_k$ is needed to update the weights. The weights at time t_0 are initialized to $\varpi_0^{(\ell)} = 1/M$ for $\ell = 1, 2, \ldots, M$. The convergence properties of MMAE are shown in Ref. [11], which assumes ergodicity in the proof. The ergodicity assumptions can be relaxed to asymptotic stationarity and other assumptions are even possible for non-stationary situations.[12]

From Eq. (33) and Eq. (31) we can see that models that have lower residuals will have probability that will increase, this will favor models that fit the observations better. Also from Eq. (31) we can see that models that have small values for $\det(S_k^{(\ell)})$ will have probability that will grow. Assuming that all models have same measurement noise covariance matrix R_k, this will favor models that have smaller variance. Therefore the MMAE process will tend to select the maximum likelihood minimum variance model from the bank of models.

ADAPTIVE LIKELIHOOD MIXTURE

The adaptive likelihood mixture (ALM) is a variation of the MMAE and interacting multiple-model approach in that it maintains less memory of the likelihood ratios of the models. The ALM approach starts by initializing each model with equal weights and updates these weights by setting them to the likelihood ratios. After the weights are updated, the individual model estimates are used to calculate an overall estimate via a weighted sum of the individual models. Following this the overall estimate is fed back into the individual models and used as the current estimate for each model. This approach weights models based on their current performance and how well they fit the current data sample and by feeding back the best estimate it ensures that each model's state prediction is near the best model.

Over very short propagation intervals the ALM will tend to equalize all the models since they will be re-initialized with the same state estimate as the weight update. Since the propagation time is short the models will not deviate much from each other and will have very similar likelihoods. However for long propagation intervals the difference between the models will become more apparent and the likelihood ratio will be fairly different. Therefore the likelihood ratios do not vary much for a given track of data. But with disparate tracks the approach will be very sensitive to detecting changes in the models.

The ALM approach is now summarized:

1. Initialization of probabilities

$$\varpi_0^{(\ell)} = 1/M$$

2. Update weights based on likelihood of models

$$\begin{aligned} \varpi_k^{(\ell)} &= p\left(\tilde{\mathbf{y}}_{k-1}|\hat{\mathbf{x}}_{k-1}^{+(\ell)}\right) \\ \varpi_k^{(\ell)} &\leftarrow \frac{\varpi_k^{(\ell)}}{\sum_{j=1}^{M} \varpi_k^{(j)}} \end{aligned} \tag{34}$$

3. Forming state estimate from individual models

$$P_k^+ = \sum_{j=1}^{M} \varpi_k^{(j)} \left(P_k^{+(j)} + \left[\bar{\mathbf{x}}_k^{+(j)} - \bar{\mathbf{x}}_k^+ \right] \left[\bar{\mathbf{x}}_k^{+(j)} - \bar{\mathbf{x}}_k^+ \right]^T \right) \tag{35}$$

$$\bar{\mathbf{x}}_k^+ = \sum_{j=1}^{M} \varpi_k^{(j)} \bar{\mathbf{x}}_k^{+(j)} \tag{36}$$

4. Resetting individual models

$$\bar{\mathbf{x}}_k^{+(j)} = \bar{\mathbf{x}}_k^+$$
$$P_k^{+(j)} = P_k^+$$

Note that the weight update does not depend on the weights from the previous time step but just the likelihood of the model at the current time step. This creates a multiple model that has no memory and can adapt to abrupt changes in the models.

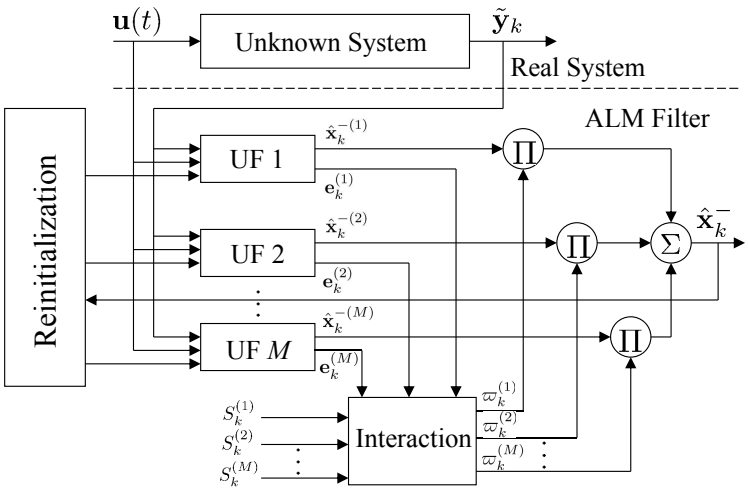

Figure 4. ALM Process

NUMERICAL EXAMPLE

Three simulations scenarios are presented: in scenario I the model bank is such that the true model is present in the bank and simple cannonball dynamics, Eq. (16), are used for both the true and estimators models; in scenario II the true model is not in the bank and simple cannonball dynamics are used for both the true and estimator models; and in scenario III the true model is not in the bank and simple cannonball dynamics are used for the estimator but true model and measurement data are generated using a cube shape model and general SRP force given in Eq. (18). In all cases the same initial attitude, position, velocity and angular velocity are used. For the generation of data for the true model, an equatorial ground station is chosen as the site of the observer. The SO is simulated to fly in a near-geosynchronous orbit in a trajectory that is continuously lighted. This is accomplished

by inclining the orbit by 15 degrees and choosing an appropriate time of the year, thereby avoiding the shadow cast by the Earth.

The initial inertial position and velocity are chosen as $\mathbf{r}^I = [-7.8931\times10^2 \;\; 3.6679\times10^4 \;\; 2.1184\times 10^4]^T$ km and $\mathbf{v}^I = [-3.0669 \;\; -4.9425\times10^{-2} \;\; -2.8545\times10^{-2}]^T$ km/s. The geographic position of the ground site is 0° North, 172° West with 0 km altitude. The time of the start of the simulation is May 8, 2007 at 5:27.55.

For all simulations scenarios, measurements are produced using zero-mean white-noise error processes with standard deviation of 0.5 arc-seconds for azimuth and elevation. The initial errors for the states are 1 km and 0.001 km/s for the position and the velocity errors, respectively. The initial condition error-covariance values are set to 1^2 km^2 and 0.001^2 (km/s)^2 for the position and the velocity errors, respectively. The time interval between the measurements is set to 20 seconds. Data is simulated for 14 nights (about 14 orbits) where observations of the SO are made every two nights for 5 minutes. The simulation results are plotted versus number of data samples since there are large time gaps between each 5 minutes data arc.

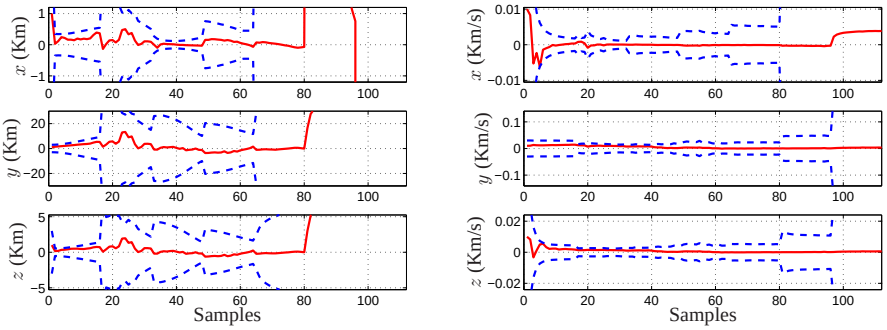

(a) Position Estimation Error (b) Velocity Estimation Error

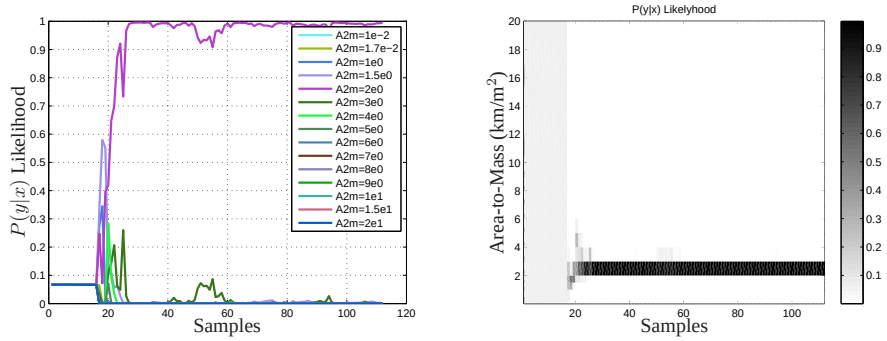

(c) Probabilities Time Series (d) Probabilities Contour Plot

Figure 5. MMAE Results for Scenario I

Scenario I

Scenario I shows the case where the model is given to the model bank and the multiple model approach attempts to identify the correct model for the bank of hypothesized models. Figures 5 and 5 show the simulation results for the MMAE and ALM, respectively. The results show position errors, velocity errors and the probabilities over time.

From Figure 5(c) the MMAE approach selects the correct model after over 20 data samples which is approximately just over one track of data. Since the tracks are separated by 2 days the models have enough time after the first data track for a model difference to develop. Once the new track of data is accepted the probabilities very quickly jump to the correct model since the predicted states of the incorrect model differ from the measurements of the new track. Figure 5(d) shows the probability contours for the area-to-mass ratio, this figure gives an indication of the probability distribution of the area-to-mass ratio parameter space. From Figure 5(d) it can be seen that the uncertainty in the area-to-mass ratio parameter reduces over time but fluctuates slightly.

Figure 6(c) shows the probabilities time series for the ALM approach and it can be seen from this figure that it takes a bit longer for the ALM approach to converge to the correct model since it is designed to detect abrupt changes and therefore has very limited memory. Figure 6(d) shows the contours for the ALM approach. From this figure we can see that the probabilities are equalized during tracks but change at the beginning of a new track when there is an abrupt change in the data (since the tracks are separated by two days in time a large change is given between time propagations). The state errors for the ALM approach are within the 3 σ bounds and show good performance.

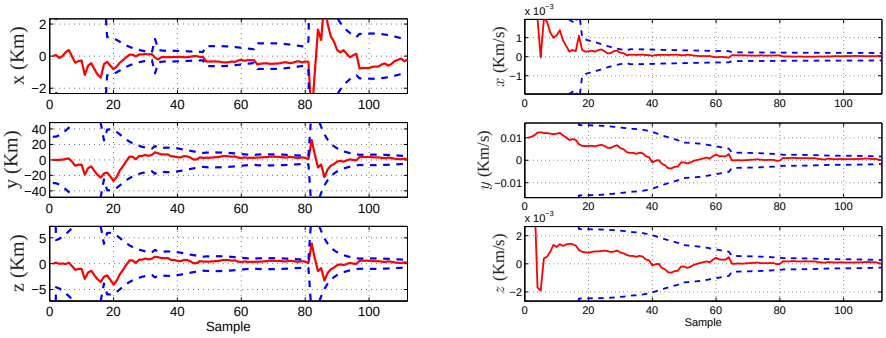

(a) Position Estimation Error

(b) Velocity Estimation Error

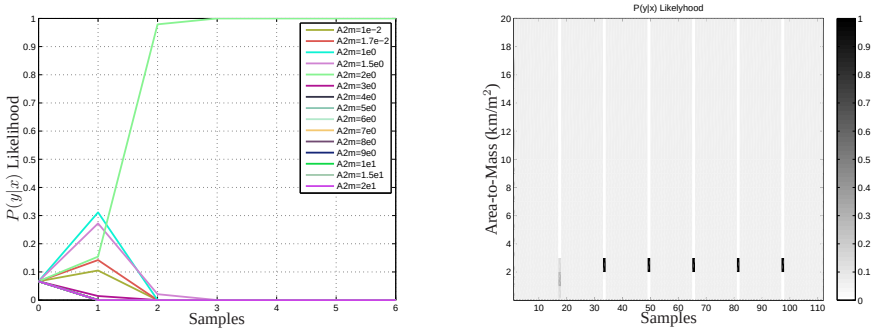

(c) Probabilities Time Series

(d) Probabilities Contour Plot

Figure 6. ALM Results for Scenario I

Scenario II

Scenario II considers the case where the actual area-to-mass ratio model is not in the bank. In this case the true area-to-mass ratio is 2.8 m^2/kg and the closest model in the bank is 2.8 m^2/kg. The

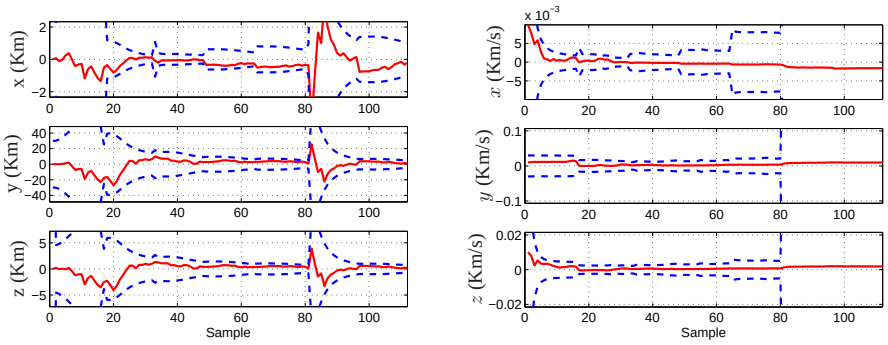

(a) Position Estimation Error (b) Velocity Estimation Error

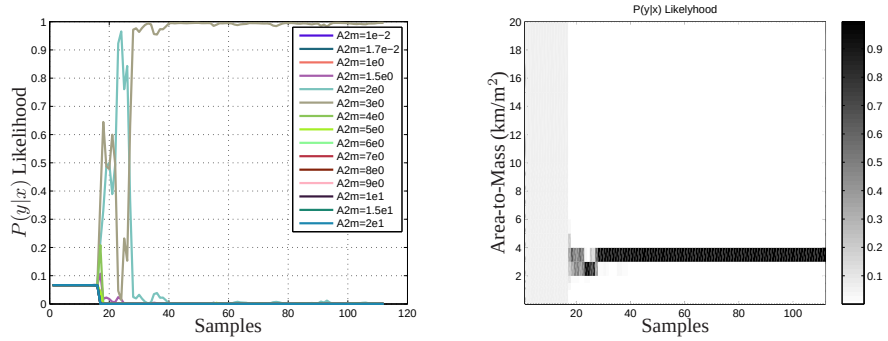

(c) Probabilities Time Series (d) Probabilities Contour Plot

Figure 7. MMAE Results for Scenario II

MMAE results for scenario II are shown in Figure 7 where it can be see that the MMAE determines the most probable model as the model with an area-to-mass ratio of 2 m^2/kg. The position and velocity estimates for the MMAE approach are within the 3 σ bounds and show good performance. The results for the ALM approach are shown in Figure 8. From Figure 8(c) it can be see that the ALM approach correctly identifies the most probable model. The position and velocity state estimates for the ALM approach are shown in Figures 8(a) and 8(b), and the estimates for the ALM approach are within the 3 σ bounds and show good performance.

Scenario III

Scenario III studies the case where the SO shape model is not a simple cannonball model but rather more complex. A faceted model is considered for this simulation where the shape model parameters as discussed previously are given by $a = 8.9443$ m, $d = 8.9443$ m, and $l = 7.8262$ m. The mass of the SO is given by mass $= 1.5kg$ and this results in an effective area-to-mass ratio for each side given by A2M $= [0.1201 \;\; 0.1201 \;\; 0.1201 \;\; 0.1201 \;\; 2.5202 \;\; 2.5202]^T$.

The initial true quaternion attitude mapping from the inertial frame to the body frame is chosen as $\mathbf{q}_I^B = [1/2 \;\; 0 \;\; 0 \;\; 1/2]^T$. A constant rotation rate, defined as the body rate with respect to the inertial frame, represented in body coordinates, is used and given by $\boldsymbol{\omega}_{B/I}^B = [0 \;\; 0.00262 \;\; 0]^T$ rad/s. A constant rotation rate, defined as the body rate with respect to the inertial frame, represented in body coordinates, is used and given by $\boldsymbol{\omega}_{B/I}^B = [0 \;\; 0.00262 \;\; 0]^T$ rad/s.

The SRP model for faceted plates given by Eq. is used to simulate the trajectory of the SO and

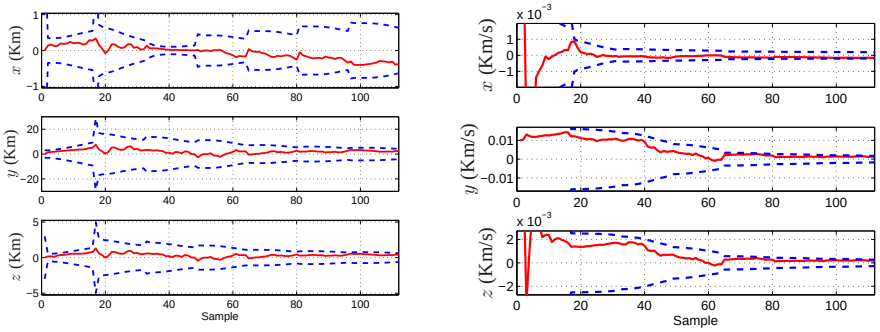

(a) Position Estimation Error (b) Velocity Estimation Error

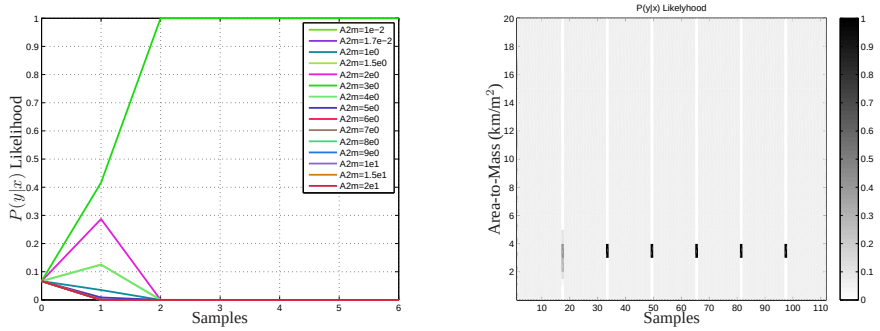

(c) Probabilities Time Series (d) Probabilities Contour Plot

Figure 8. ALM Results Scenario II

from the simulated trajectory synthetic data are generated. The model in both the MMAE and ALM approach use simplified cannonball models where the SRP force is not a function of the orientation of the SO. Therefore the models in the bank will attempt to approximate the more complex truth models that generate the data.

The MMAE results for scenario III are shown in Figure 9 where is can be see that the MMAE determinea the most probable model over time as models with an area-to-mass ratio of 2 m^2/kg which the highest area-to-mass for the flat plate shape model. The position and velocity estimates for the MMAE approach are within the 3 σ bounds and show good performance. The results for the ALM approach are shown in Figure 10. From Figure 10(c) it can be see that the ALM approach correctly identifies the most probable model. The position and velocity state estimates for the ALM approach are shown in Figures 10(a) and 10(b), and the estimates for the ALM approach are within the 3 σ bounds and show good performance.

CONCLUSION

In this paper a bank of unscented Kalman filters are used to estimate the position of a space object (SO) using angles data and hypothesizing on the area-to-mass ratio for each model. This approach is used to detect abrupt changes in the area-to-mass ratio that will allow improved state estimation without the use of process noise to account for the un-modeled changes in the effective area-to-mass ratio. This work presented two multiple models approach applied to the area-to-mass ratio estimation problem. The first approach is the well known multiple-model adaptive estimation

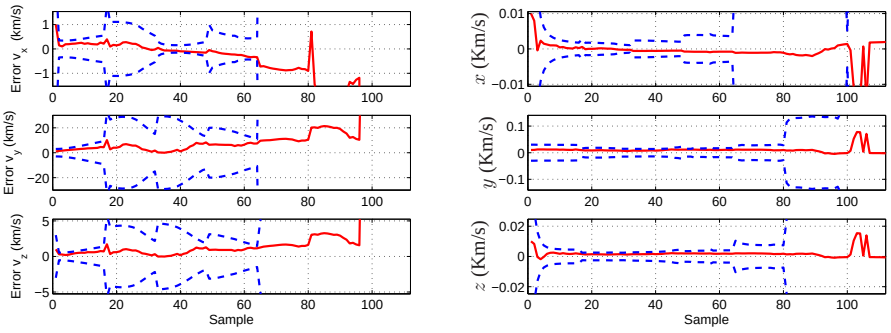

(a) Position Estimation Error

(b) Velocity Estimation Error

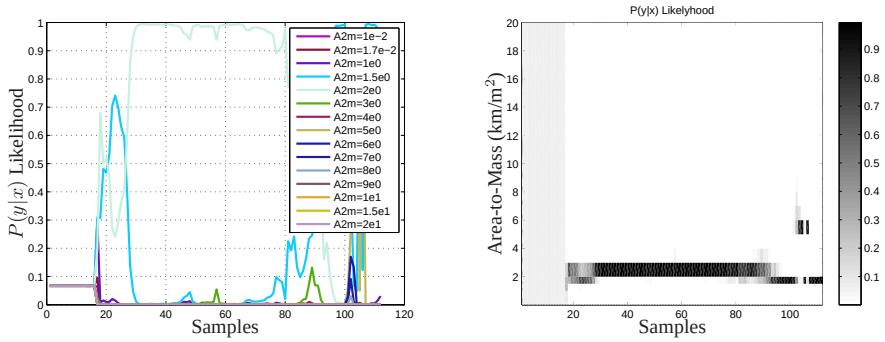

(c) Probabilities Time Series

(d) Probabilities Contour Plot

Figure 9. MMAE Results for Scenario III

(MMAE) approach and the second approach was proposed for this work is called adaptive likelihood mixture (ALM). The ALM approach removed the memory of the MMAE by basing the weights of each model on the current likelihood ratios of the models which not dependent on the previous weights. The usefulness of the ALM approach is that it can detect abrupt changes in the data. In the case where un-modeled effects cause changes in effective area-to-mass ratio the ALM can detect these changes faster than the MMAE approach. Simulation scenarios are presented in this work and are used to show the effectiveness of the proposed approaches for detecting the area-to-mass ratio of a SO and compensating for un-modeled effects that create changes in the effective area-to-mass ratio. It is shown that the multiple model approaches can correctly identify the correct area-to-mass ratio model when it is given in the bank and can find the most probable model if this model is not in the bank. It is also shown that if the true model is not a cannonball shape that the multiple model approaches can find the most probable effective area-to-mass ratio using the bank of models. The state estimation errors and 3σ bounds show that the multiple model approaches provide consistent results.

REFERENCES

[1] Schildknecht, T., "Optical Surveys for Space Debris," *Astronomy and Astrophysics Review*, Vol. 14, No. 1, 2007, pp. 41–111.

[2] Kelecy, T. and Jah, M., "Analysis of High Area-to-Mass Ratio (HAMR) GEO Space Object Orbit Determination and Prediction Performance: Initial Strategies to Recover and Predict HAMR GEO Trajectories with No a priori Information," *Acta Astronautica*, Vol. 69, No. 7-8, Sept. 2011, pp. 551–558.

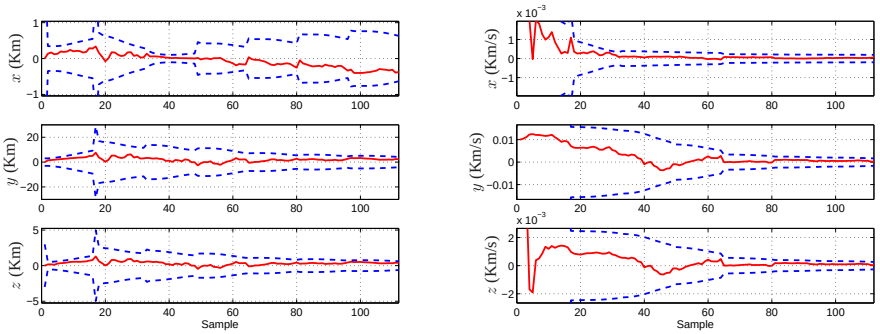

(a) Position Estimation Error (b) Velocity Estimation Error

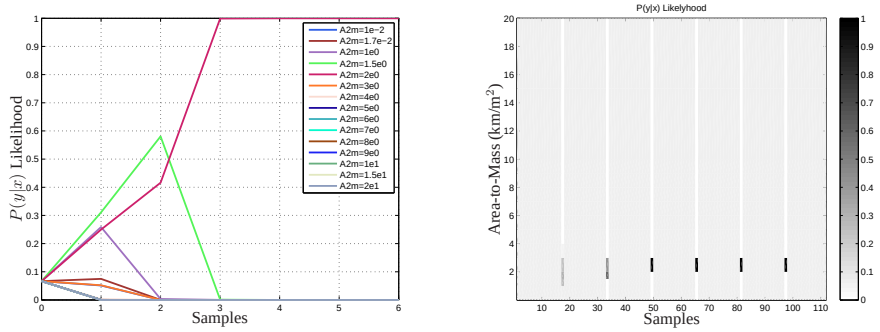

(c) Probabilities Time Series (d) Probabilities Contour Plot

Figure 10. ALM Results for Scenario III

[3] Linares, R., Crassidis, J. L., Jah, M., and Kim, H., "Astrometric and Photometric Data Fussion for Orbit, Attitude, and Shape Estimation," *AIAA Guidance, Navigation and Control Conference*, Chicago, IL, Aug. 2010, AIAA-2009-6293.

[4] Jazwinski, A. H., *Stochastic Processes and Filtering Theory*, chap. 8, Academic Press, San Diego, CA, 1970.

[5] Julier, S. J., Uhlmann, J. K., and Durrant-Whyte, H. F., "A New Method for the Nonlinear Transformation of Means and Covariances in Filters and Estimators," *IEEE Transactions on Automatic Control*, Vol. AC-45, No. 3, March 2000, pp. 477–482.

[6] Gordon, N. J., Salmond, D. J., and Smith, A. F. M., "Novel Approach to Nonlinear/Non-Gaussian Bayesian State Estimation," *IEE Proceedings, Part F - Communications, Radar and Signal Processing*, Vol. 140, No. 2, Seattle, WA, April 1993, pp. 107–113.

[7] Shuster, M. D., "A Survey of Attitude Representations," *Journal of the Astronautical Sciences*, Vol. 41, No. 4, Oct.-Dec. 1993, pp. 439–517.

[8] Ashikmin, M. and Shirley, P., "An Anisotropic Phong Light Reflection Model," Tech. Rep. UUCS-00-014, University of Utah, Salt Lake City, UT, 2000.

[9] Brown, R. G. and Hwang, P. Y. C., *Introduction to Random Signals and Applied Kalman Filtering*, John Wiley & Sons, New York, NY, 3rd ed., 1997, pp. 353–361.

[10] Stengel, R. F., *Optimal Control and Estimation*, Dover Publications, New York, NY, 1994, pp. 402–407.

[11] Anderson, B. D. O. and Moore, J. B., *Optimal Filtering*, chap. 10.1, Dover Publications, Mineola, NY, 2005.

[12] Anderson, B. D. O., Moore, J. B., and Hawkes, R. M., "Model Approximations via Prediction Error Identification," *Automatica*, Vol. 14, No. 6, Nov. 1978, pp. 615–622.